Journal of Materials Chemistry B

PAPER

View Article Online
View Journal | View Issue

Cite this: J. Mater. Chem. B, 2018, 6, 4937

Novel iron oxide–cerium oxide core–shell nanoparticles as a potential theranostic material for ROS related inflammatory diseases†

Yuao Wu,[a] Yanchen Yang,[a] Wei Zhao,[a] Zhi Ping Xu,[a] Peter J. Little,[b] Andrew K. Whittaker,[acd] Run Zhang[a] and Hang T. Ta*[ab]

Received 4th January 2018,
Accepted 26th June 2018

DOI: 10.1039/c8tb00022k

rsc.li/materials-b

Reactive oxygen species (ROS) and reactive nitrogen species (RNS) are key signaling molecules that play an important role in the inflammation and progression of many diseases such as cardiovascular disease, especially atherosclerosis. ROS are in particular a significant factor in the development of rheumatoid arthritis and other autoimmune diseases such as allergies. In this study, novel Fe_3O_4/CeO_2 core–shell theranostic nanoparticles capable of reacting with ROS and of being detected by MRI were synthesized and thoroughly characterized. *In vitro* studies, such as measurement of cell uptake, magnetic resonance imaging, toxicity and ROS scavenging, were conducted. The results indicate that the novel Fe_3O_4/CeO_2 theranostic nanoparticles are effective for scavenging ROS and show excellent magnetic resonance (MR) imaging performance. These theranostic nanomaterials, therefore, show great potential for the treatment and diagnosis of ROS-related inflammatory diseases.

Introduction

Inflammatory diseases comprise a group of diseases that involve the body's immune system. Diseases such as rheumatoid arthritis and atherosclerosis affect many millions of people every year. For example, atherosclerosis, the most prevalent cardiovascular disease, may cause ischemic heart disease and cerebrovascular disease (stroke).[1] In 2013, ischemic heart disease and cerebrovascular disease were claimed to be the world's first and third cause of death, causing 137 and 110 deaths per every 100 000 people, respectively.[2] Also, more than half of patients with rheumatoid arthritis are incapable of holding a full-time job as a direct consequence of the disease.[3]

Reactive oxygen species (ROS) production is one of the main reasons for the progression of many inflammatory diseases. ROS include hydrogen peroxide (H_2O_2), superoxide, and hydroxyl radicals as well as their reactive products; these molecules contain a high level of reactive oxygen described as harmful products of metabolism.[4] Among these, H_2O_2 is the most important ROS in redox signaling. In addition, it is the most studied and the best-characterized member of ROS.[5] Due to their oxidization capability, ROS are able to damage important molecules in our bodies, such as lipid peroxidation, DNA mutation, and protein dysfunction.[5,6] Therefore, ROS are key signaling molecules that play an important role in the progression of inflammatory disorders. In addition to their potential harm, it is reported that ROS are regulators of cell signaling and immune responses.[7]

There are four kinds of ROS in the inflammation diseases, the most important of which is NADPH oxidase-derived ROS that relates to both atherosclerosis[5,8] and rheumatoid arthritis.[6] Besides, there are also mitochondrial-derived ROS,[5,9] uncoupled nitric oxide synthase-derived ROS[10] and xanthine oxidoreductase derived ROS[11] in inflammatory diseases. Under the inflammatory conditions, the oxidative stress produced by polymorphonuclear neutrophils such as macrophages leads to the formation of inter-endothelial junctions, accelerating the migration of inflammatory cells across the endothelial barrier, which makes the situation worse in atherosclerosis and rheumatoid arthritis patients.[12,13] In atherosclerosis, ROS is produced by macrophages and endothelial cells during the process of the plaque, and it is the key factor of the accumulation of oxidized low-density lipoprotein in the intima of the blood vessel.[14,15] In rheumatoid arthritis, the relevant ROS including nitric oxide (NO) and superoxide anion (O^{2-}) are produced by chondrocytes followed by the generation of derivative radicals, such as hydrogen peroxide (H_2O_2).[16,17] Therefore, an effective antioxidant compound, which can reduce ROS in the inflammatory cells, could be a key factor for the treatment of chronic inflammatory disease.

[a] Australian Institute for Bioengineering and Nanotechnology, The University of Queensland, Brisbane, Australia. E-mail: h.ta@uq.edu.au, hangthuta@gmail.com
[b] School of Pharmacy, The University of Queensland, Brisbane, Australia
[c] Australian Research Council Centre of Excellence in Convergent Bio-Nano Science and Technology, Brisbane, Australia
[d] Centre for Advanced Imaging, The University of Queensland, Brisbane, Australia

† Electronic supplementary information (ESI) available. See DOI: 10.1039/c8tb00022k

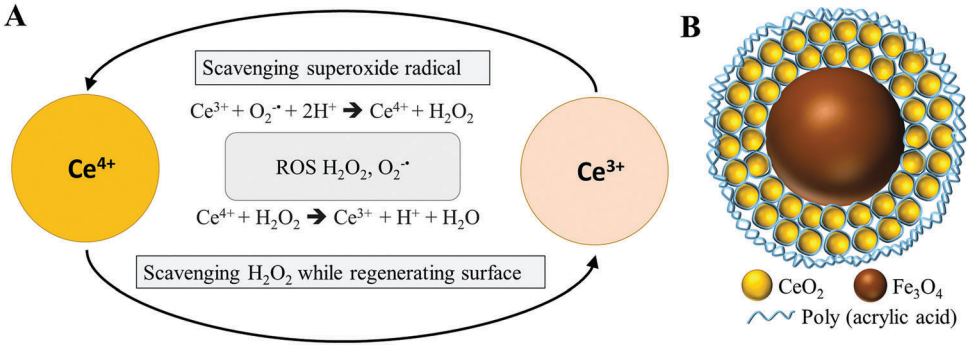

Fig. 1 Regenerative antioxidant properties of cerium oxide and the simulation structure of iron oxide/cerium oxide core–shell nanoparticles (IO@CO). (A) Regenerative antioxidant properties of cerium oxide show that cerium ions are capable of scavenging superoxide radicals when the trivalent cerium ions change to tetravalent cerium ions.[21] On the other hand, it has the ability of scavenging H_2O_2 when tetravalent cerium ions become trivalent cerium ions. (B) Simulation structure of iron oxide/cerium oxide core–shell nanoparticles (IO@CO).

Cerium compounds have been used as traditional drugs for inflammation over the last two hundred years. The first publication of cerium used as drugs can trace back to the 1850s. Originally, the trivalent ions of cerium were used to treat bacterial infections, sepsis and inflammatory responses in patients with fire burns.[18] In 2007, Korsvik *et al.* demonstrated that higher levels of Ce^{3+} than Ce^{4+} on the surface of a particle are more likely to act as superoxide dismutase, which accelerates the dismutation of superoxide radical to O_2 or H_2O_2.[19] This ability of the anti-superoxide radical is supported by another study claiming that a high Ce^{3+}/Ce^{4+} ratio of nanoparticles contributes more superoxide dismutase activities than a low Ce^{3+}/Ce^{4+} ratio.[20] The potential mechanism of the unique regeneration antioxidant properties of cerium oxide is illustrated in Fig. 1A, which results from the switch between Ce^{3+} and Ce^{4+} on the surface of the nanoparticle.[21,22] Therefore, cerium oxide nanoparticles with their unparalleled antioxidant properties are potential radical scavengers and redox cycling antioxidants.

Superparamagnetic iron oxide nanoparticles (SPIONs) are small synthetic particles with Fe_2O_3 or Fe_3O_4 cores. SPIONs usually range between 10 nm and 100 nm in diameter and are excellent contrast agents for magnetic resonance imaging.[23] SPIONs are usually coated with biocompatible polymers, such as polyethylene glycol, limiting their interaction with substances in the surrounding environment and enhancing their stability under physiological conditions.[24] In ROS related inflammatory diseases, molecule markers such as chemokines, cytokines and other adhesion molecules take part in the inflammation process.[25] Recently, in atherosclerosis,[26] iron oxide nanoparticles functionalized with binding ligands that target atherosclerosis biomarkers have been widely studied in molecular magnetic resonance imaging (MRI) of atherosclerosis.[17,18] SPIONs can be a potential imaging agent for diagnosing inflammatory diseases as well as monitoring treatment of these diseases.

Nanotechnology has taken the most important place in the development of theranostics that exhibits not only effective therapy, but also imaging for many diseases such as cancer and inflammatory diseases.[27,28] Basically, theranostic nanoparticles are capable of loading large amounts of therapeutic and imaging agents as well as binding functional targeting ligands at the surface, which can increase the therapeutic and imaging efficacy while reducing off-site toxicity.[29] Functionalization of theranostic nanoparticles can modulate the drug release related to the internal environments in our bodies such as temperature, enzymes, the potential of hydrogen (pH) value and redox potential.[30] The half-life time of theranostic nanoparticles can be enhanced by modification of the surface by hydrophilic polymers such as poly(acrylic acid) (PAA).[29] Theranostic nanomaterials combine both diagnostic and therapeutic capabilities in one dose, and also allow the tracking or monitoring of drug delivery to the disease site.

In this study, we have synthesized a novel theranostic nanoparticle comprising an iron oxide (core) and cerium oxide (shell) (Fig. 1B) as a potential theranostic nanomaterial for ROS related inflammatory diseases. This innovative nanomaterial simultaneously provides both diagnostic capability *via* iron oxide (MR imaging agent) and therapeutic functionality *via* cerium oxide (anti-ROS capability) in one dose. This combination is also expected to allow the tracking of cerium oxide delivery to the disease site and enable its biodistribution evaluation. The characterization studies indicated that these iron oxide–cerium oxide core–shell nanoparticles (IO@CO) are good contrast agents for MRI. *In vitro* studies showed that our nanoparticles have a significant anti-ROS ability with good cell uptake and low cytotoxicity. These IO@CO nanoparticles could be a potential agent for the diagnosis and treatment of ROS-related inflammatory diseases such as atherosclerotic plaques and rheumatoid arthritis.

Experimental section

Materials

Iron chloride, sodium oleate, polyoxyethylene (5) nonylphenyl ether (Igepal CO-520), cerium nitrate hexahydrate, urea, poly(acrylic acid) (PAA, M_w = 1800), hydrogen peroxide (H_2O_2), 2,2′-azino-bis(3-ethylbenzothiazoline-6-sulphonic acid) (ABTS), horseradish peroxidase (HRP) and 2′,7′-dichlorodihydrofluorescein

diacetate (DCFH-DA) were purchased from Sigma-Aldrich. Water used in all experiments was Milli-Q water. Phosphate-buffered saline (PBS), RPMI 1640 medium, fetal calf serum, penicillin–streptomycin solution, L-glutamine, non-essential amino acids solution (100×) and TrypLE™ Express were purchased from ThermoFisher Scientific. Ethidium homodimer-1 fluorescent dye was purchased from Molecular Probes™.

Synthesis of the iron–oleate complex

Iron–oleate complexes were synthesized according to a previous report.[31] Typically, 44.6 g of sodium oleate (120 mmol, ≥82%) and 10.8 g of iron chloride ($FeCl_3 \cdot 6H_2O$, 40 mmol, 98%) was dissolved in a solvent mixture of 80 mL ethanol, 60 mL distilled water and 140 mL hexane. The resulting solution was heated to 70 °C and kept at this temperature for four hours. When the reaction was completed, the upper organic layer containing the iron–oleate complex was washed three times with 30 mL distilled water in a separatory funnel. After washing, hexane was evaporated off, resulting in the iron–oleate complex in a viscous liquid form.

Synthesis of iron oxide nanoparticles

Fe_3O_4 nanoparticles with a core size of 10 nm were synthesized according to a previous report with slight modifications.[32] Typically, 3.6 g (4 mmol) of freshly prepared iron oleate and 3.39 g (4 mmol) of oleic acid were dissolved in 25 mL of 1-octadecence. The resulting solution was degassed for 10 min using argon and then was heated to 310 °C for 1 hour under argon protection. The preparation was terminated by cooling the reaction mixture to room temperature (RT). The nanoparticles were washed three times by precipitation with ethanol and redispersion in cyclohexane.

Synthesis of iron oxide/cerium oxide core–shell nanoparticles (IO@CO)

Synthesis of IO@CO1 (NaOH used as precipitation agent). Reverse micelle systems were used to synthesize IO@CO nanoparticles. Firstly, a $Fe_3O_4/Ce(NO_3)_3$ reverse micelle solution was prepared as follows: 0.96 g Igepal CO-520 (2.185 mmol) (sonication for 30 min after adding into cyclohexane) and 0.6 mg Fe_3O_4 nanoparticles were dispersed in 10.5 mL of cyclohexane and gently stirred for 2 h at RT. After 2 h, 0.04 g $Ce(NO_3)_3 \cdot 6H_2O$ (0.92 M) was dispersed in 100 μL water, and the solution was labeled as mixture A. Then, 100 μL of mixture A was added to the above solution and the mixture was vigorously stirred for 2 hours. Secondly, a NaOH reverse micelle solution was prepared as follows: 0.48 g Igepal CO-520 (1.0925 mmol) (sonication for 30 min after adding into cyclohexane) was dispersed in 5.25 mL of cyclohexane. Then, solution B containing 50 μL aq. NaOH (1.5 M) was added to the above mixture and the solution was vigorously stirred for 2 h at RT. The two reverse micelle solutions were blended and incubated overnight at RT with stirring at 250 rpm. After 24 h, the poly(acrylic acid) reverse micelle solution was prepared as follows: 0.48 g of Igepal CO-520 (1.0925 mmol) (sonication for 30 min after adding into cyclohexane) was dispersed in 5.25 mL of cyclohexane. Next, 2 mg poly(acrylic acid) dissolved in 50 μL water was added to the reaction solution, and the solution was stirred vigorously for 2 h at RT. After 2 h, the poly(acrylic acid) reverse micelle solution was added to the mixture of two reverse micelle solutions that had been incubated overnight. The mixture containing three reverse micelle solutions was stirred overnight at 250 rpm. After that, the nanoparticles were precipitated by adding 2 mL methanol and separated by high speed centrifugation (20 000 rpm, 15 min, 22 °C). The precipitate was washed twice with 1 mL ethanol and subsequently washed once with a mixture of water and ethanol (500 μL: 500 μL). The resulting nanoparticles (IO/CONP1) were washed by dialysis, and then concentrated and redispersed in 100 μL water. Scheme 1 illustrates the synthesis protocol of IO@CO1.

Synthesis of IO@CO2 (urea used as precipitation agent). Firstly, an $Fe_3O_4/Ce(NO_3)_3/(NH_2)_2CO$ reverse micelle solution was prepared as follows: 0.96 g Igepal CO-520 (2.185 mmol) (sonication for 30 min after adding into cyclohexane) and 0.6 mg Fe_3O_4 nanoparticles were dispersed in 10.5 mL of cyclohexane and gently stirred for 2 h at RT. After 2 h, 0.005 g $Ce(NO_3)_3 \cdot 6H_2O$ (0.58 M) and 0.0075 g $(NH_2)_2CO$ (6.2 M) were dispersed in 20 μL water, and the solution was labeled as mixture A. Then 20 μL of mixture A was added to the above solution, and the solution was vigorously stirred for 2 h. After 2 h, the mixture was heated at 60 °C overnight with gentle stirring. After 24 h, the poly(acrylic acid) reverse micelle solution was prepared as follows: 0.48 g Igepal CO-520 (1.0925 mmol) (sonication for 30 min after adding into cyclohexane) was dispersed in 5.25 mL of cyclohexane. Next, 2 mg poly(acrylic acid) dissolved in 50 μL water was added to the reaction solution, and the solution was stirred for 2 h at RT. The two reverse micelle solutions were mixed together and vigorously stirred for 2 h. Then, the stirring speed was reduced to 250 rpm and the reaction solution was incubated overnight at RT with gentle stirring. After that, the following steps were the same as that of IO/CO1, including precipitation, washing, dialysis and concentrating. Finally, the nanoparticles (IO@CO2) were redispersed in 100 μL water. Scheme 2 illustrates the synthesis of IO@CO2.

Characterisation of nanoparticles

Transmission electron microscopy (TEM) images were taken on a JEOL-JEM-1010 transmission electron microscope operating at an accelerating voltage of 100 kV. Hydrodynamic size, size distribution and zeta potential (ZP) of the nanoparticles were determined using a Zetasizer Nano ZS (Malvern). The iron and cerium concentrations of IO@CO were determined using inductively coupled plasma-optical emission spectroscopy (ICP-OES) (Optima 8300DV ICP-OES from Perkin Elmer). Fourier transform infrared (FTIR) spectra were recorded using a Nicolet 5700 FT-IR spectrometer. The surface composition of the nanoparticle was analyzed by X-ray photoelectron spectroscopy (XPS) using a Kratos Axis Ultra photoelectron spectrometer. The T_1 relaxation time of the nanoparticles was recorded on an Avance 400 MHz spectrometer. The T_2 relaxation time and magnetic resonance imaging (MRI) of nanoparticles were acquired using

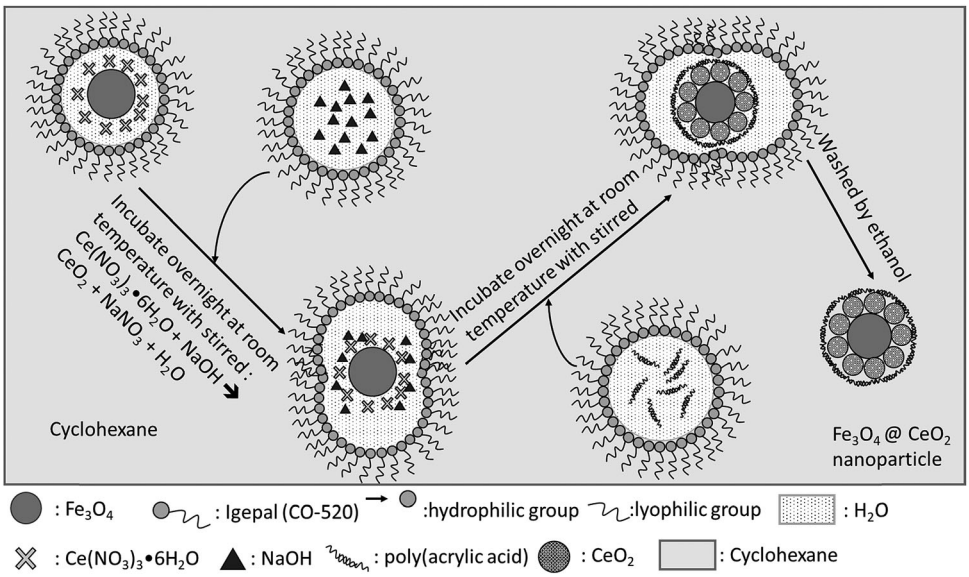

Scheme 1 Image illustrating the synthesis of IO@CO1. The protocol including (1) Igepal CO-520 and Fe_3O_4 nanoparticles were dispersed in cyclohexane and stirred for 2 h at RT. $Ce(NO_3)_3{\cdot}6H_2O$ was added into the above solution and stirred for another 2 h at RT. (2) Igepal CO-520 and NaOH were dispersed in cyclohexane and stirred for 2 h at RT. The first and second solutions were mixed and incubated overnight at RT with stirring. (3) Igepal CO-520 and poly(acrylic acid) were stirred for 2 h at RT and added into the above mixed solution. The mixture was then incubated overnight at RT with stirring. After incubation, the nanoparticles were washed and redispersed in water.

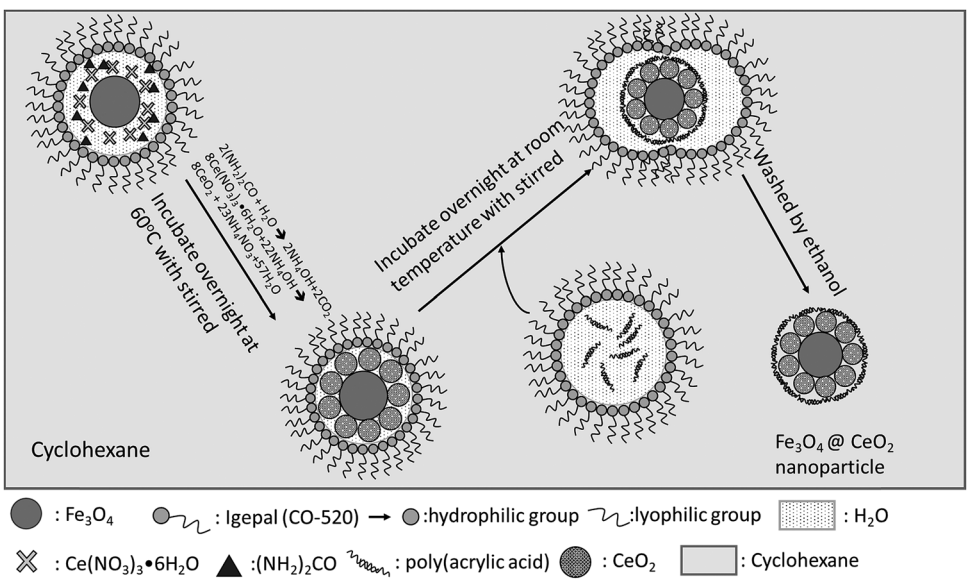

Scheme 2 Image illustrating the synthesis of IO@CO2. The protocol including (1) Igepal CO-520 and Fe_3O_4 nanoparticles were dispersed in cyclohexane and stirred for 2 h at RT. $Ce(NO_3)_3{\cdot}6H_2O$ and $(NH_2)_2CO$ were added and stirred for another 2 h at RT. (2) The solution was incubated for 24 h at 60 °C with stirring. After that, Igepal CO-520 and poly(acrylic acid) were stirred for 2 h at RT and then added into the above solution and stirred for another 2 h. The synthesised nanoparticles were washed and redispersed in water.

a Bruker 9.4 T MRI scanner. T_2-weighted relaxivity (r_2) is generally defined as the slope of the linear regression generated from a plot of the measured relaxation rate ($1/T_2$) *versus* the concentration of the contrast agent (iron, Fe).

Anti-ROS capability of IO@CO nanoparticles

Nanoparticles of different cerium (Ce) concentrations (0 μg mL^{-1}, 0.0028 μg mL^{-1}, 0.028 μg mL^{-1} 0.28 μg mL^{-1}, 2.8 μg mL^{-1}, 5.6 μg mL^{-1} and 11.2 μg mL^{-1}) were treated with 0.1 mM H_2O_2 in a 96-well plate for 1 h at 37 °C with shaking (200 rpm). 0.01 unit of HRP was added into each reaction, followed by 10 min incubation at RT. 8.7 mM ABTS was then added into the reaction and the absorbance of the samples at 405 nm was measured using a microplate reader Tecan X200. The absorbance of a 0 μg mL^{-1} sample was determined as 0% ROS scavenging.

Cell culture

Macrophage J774A.1 was obtained from the American Type Culture Collection (ATCC). The cells were maintained in a non-treated 100 × 20 mm cell culture dish containing RPMI 1640 with fetal calf serum (10%), penicillin (100 U mL^{-1}) and L-glutamine (1%) and cultured in an incubator at 37 °C with 5% CO_2.

Cell uptake of IO@CO nanoparticles

When cell confluence reached approximately 90%, the cells were detached using cold PBS (4 °C) by a pipette. Then, the cells were transferred to a 24-well plate at a density of 40 000 cells per well. After 48 h incubation, the cells were separately treated with different concentrations of IO@CO1 and IO@CO2 ([Ce]: 0 μg mL^{-1}, 2.8 μg mL^{-1} and 5.6 μg mL^{-1}). After an additional 24 h incubation, cells in the 24-well plate were washed with 1× PBS and then lysed with 8% HNO_3 and the lysis solutions were diluted to 2% HNO_3 for inductively coupled plasma mass spectrometry (ICP-MS) (Agilent 7900 with collision cell technology) analysis. ICP-MS was used to detect the content of Fe and Ce in macrophages treated with different concentrations of the nanoparticles.

In vitro MRI

When cell confluence reached approximately 90%, the cells were detached using cold PBS (4 °C) by a pipette. Then, the cells were transferred into a 96-well plate at a density of 5000 cells per well. After 48 h incubation, the cells were separately treated with different concentrations of IO@CO1 and IO@CO2 ([Ce]: 2.8 μg mL^{-1}). After an additional 24 h incubation, the cells were washed with PBS twice and fixed by paraformaldehyde (PFA). The cells were detached by TrypLE Express and centrifuged for MRI. To prepare MRI samples, the cells were centrifuged at 200 g for 5 min in a 1.5 mL eppendorf tube and resuspended in 10 μL of a 0.5% agarose solution to make the cell-containing gel. After the solidification of the cell pellet, 0.5% agarose gel was added at the top of the cells pellet and the 1.5 mL eppendorf tube was placed in the 50 mL centrifuge tube containing 0.5% agarose gel (Scheme 3). MRI samples were prepared as shown in Scheme 3, followed by imaging using 9.4 T MRI. T_2 relaxation time was also recorded.

Cytotoxicity study

Macrophage J774A.1 cells were seeded into a 96-well plate at a density of 5000 cells per well. After 48 h incubation, the cells were treated with different concentrations of IO@CO1 and IO@CO2 ([Ce]: 0 μg mL^{-1}, 0.07 μg mL^{-1}, 0.14 μg mL^{-1} 0.28 μg mL^{-1}, 0.56 μg mL^{-1}, 1.4 μg mL^{-1}, 2.8 μg mL^{-1}, 5.6 μg mL^{-1}, 10 μg mL^{-1}, 15 μg mL^{-1} and 20 μg mL^{-1}). The cells were then treated with ethidium homodimer-1 fluorescence dye to detect dead macrophages. The fluorescence intensity was measured using a microplate reader (Tecan X200) at an excitation wavelength of 528 nm and an emission wavelength of 617 nm. The fluorescence of the 0 μg mL^{-1} sample was determined as 100% macrophage viability. Fluorescence images and bright-field images of macrophages were also taken using Olympus IX51 fluorescence microscopy with an Olympus TH4-200 visual light source and a CoolLED pE-300 fluorescent light source.

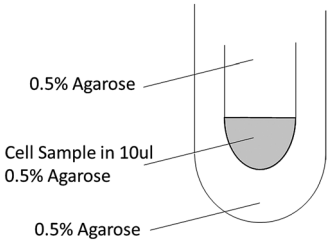

Scheme 3 Image illustrating the preparation of cell samples for MRI.

In vitro ROS scavenging cell-based assay

Macrophage J774A.1 cells were seeded into a 96-well plate at a density of 5000 cells per well. After 48 h incubation, the cells were separately treated with different concentrations of IO@CO1 and IO@CO2 ([Ce]: 0 μg mL^{-1}, 0.014 μg mL^{-1}, 0.056 μg mL^{-1}, 0.14 μg mL^{-1} and 1.4 μg mL^{-1}). After an additional 24 h incubation, the macrophages were stimulated with 1.5 mM H_2O_2 for 1 hour in an incubator at 37 °C and 5% CO_2. Intracellular ROS levels were detected by incubating the cells with 25 μM DCF_DA for 45 min in an incubator at 37 °C and 5% CO_2. The fluorescence intensity was measured by Tecan X200 (ex/em: 485/535 nm) and fluorescence images were taken using Olympus IX51 fluorescence microscopy with a CoolLED *p*E-300 fluorescent light source.

Statistical analysis of data

Data are presented as mean ± standard deviation (SD). One-way ANOVA was used in the analysis of significant difference. A p value of ≤ 0.05 was considered significant. Graphs were plotted using GraphPad Prism 7.

Results and discussion

Synthesis and characterization of IO@CO nanoparticles

Recently, "core–shell nanoparticles" have attracted scientists' attention in medical areas, such as bio-modified Fe_3O_4@Au core–shell nanoparticles for targeting and multimodal imaging of cancer cells,[33] Fe_3O_4@Au core–shell nanocomposite probes for the detection of mutation of DNA in aqueous solutions,[34] and Fe@Fe_2O_3 core–shell nanoparticles are selectively used for the detection of damaged DNA.[35] In addition, Pt@CeO_2[36] and Au@CeO_2[37] nanocomposites are used for a better interaction in biocatalysts. In our study, an iron oxide/cerium oxide core–shell (IO@CO) nanoparticle was firstly synthesized by using reverse microemulsion approaches. The TEM images (Fig. 2A) showed that the IO@CO nanoparticle comprises a 10 nm Fe_3O_4 core surrounded by spherical CeO_2 nanoparticles with approximately 2 nm diameters assembling to form the shell. IO@CO1 (~55 nm) was bigger than IO@CO2 (~22 nm) as the central iron oxide nanocore of IO@CO1 was surrounded by more CeO_2 particles than IO@CO2. IO@CO1 and IO@CO2 have hydrodynamic sizes of 55 nm and 22 nm, respectively, with low

A

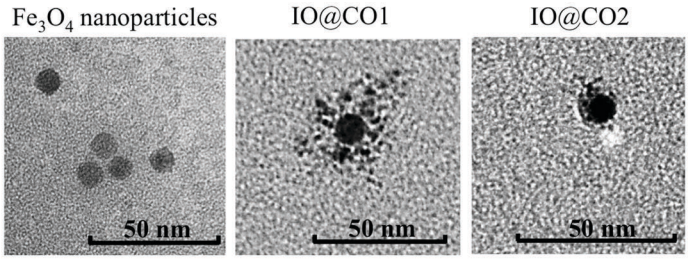

B

Sample	IO@CO1	IO@CO2
Size (mean value)	53.5±1.0	22.4±0.8
Pdi (mean value)	0.259±0.008	0.281±0.089
Zeta potential	-55.4±1.5	-53.9±0.4

C

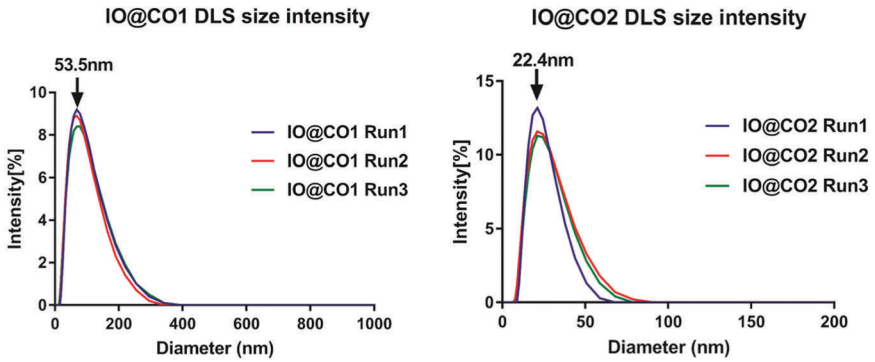

Fig. 2 Characteristics of IO@CO nanoparticles. (A) TEM images of Fe_3O_4, IO@CO1 and IO@CO2 nanoparticles. IO@CO1 has a bigger size than IO@CO2 in accordance with data from DLS zetasizer (scale bar, 50 nm). (B) Nanoparticle size and zeta potential measured by DLS zetasizer. Zeta potential data showed that both of these two nanoparticles are negatively charged. (C) DLS size distribution of the nanoparticles.

polydispersity index (PdI) (Fig. 2B). The low magnification images (Fig. S1, ESI†) and DLS size intensity graphs (Fig. 2C) showed that IO@CO has a good distribution in water. Both of the nanoparticles were highly negatively charged.

The peaks of the chemical bonds (C–H, C═O and C–O) of PAA are present in the Fourier transform infrared (FTIR) spectra of IO@CO nanoparticles, indicating that PAA was successfully coated on the nanoparticles (Fig. 3). The carboxylic acid groups in PAA are the key factor that links CeO_2 and Fe_3O_4. Clusters of CeO_2 were assembled in the presence of PAA *via* an interfacial interaction between PAA and oxide metal surfaces. This is the interactions between the proton-donating pendent COOH groups of the PAA molecules and the polar OH groups at the hydrated oxide surface sites.[38] These CeO_2 clusters were then coated around the Fe_3O_4 core *via* the same interaction mechanism between the free COOH groups on the PAA molecules and the Fe_3O_4 surface. The FTIR spectra IO@CO also showed a strong peak at around 1500 cm^{-1} that was from the iron–oleate complex. The C–O stretching at 1700 cm^{-1} in oleic acid formed a new peak at around 1550 cm^{-1} after the formation of iron–carboxylate bonds.[64]

X-ray photoelectron spectroscopy (XPS) was employed to determine the different oxidation states of cerium that are proportional to the bioactivity of the nanoparticle. As evident from Fig. 4, both trivalent cerium (Ce^{3+}) and tetravalent cerium (Ce^{4+}) oxidation states are present in the nanoparticles (Fig. 4A), which means that these nanoparticles were able to be used for further application in ROS quenching experiments. An additional result confirmed by XPS showed that IO@CO2 has a higher Ce^{3+} to Ce^{4+} ratio compared to IO@CO1 (1 : 3 and 1 : 4, respectively) (Fig. 4B).

Subsequently, we tested whether the IO@CO nanoparticle is a good MRI contrast agent. Phantoms of IO@CO nanoparticle solutions with different iron concentrations were prepared. T_2-weighted MR images of both the IO@CO1 and IO@CO2 samples were getting darker or the MRI signal of the samples decreased when the concentration of iron oxide increased. Fig. 5A shows that IO@CO2 has a stronger T_2 contrast effect. Fig. 5B and C also indicate that IO@CO2 has a higher T_2-weighted relaxivity (r_2) than IO@CO1 (378 and 339 mM^{-1}, s^{-1}, respectively). IO@CO2 showed a steeper slope of

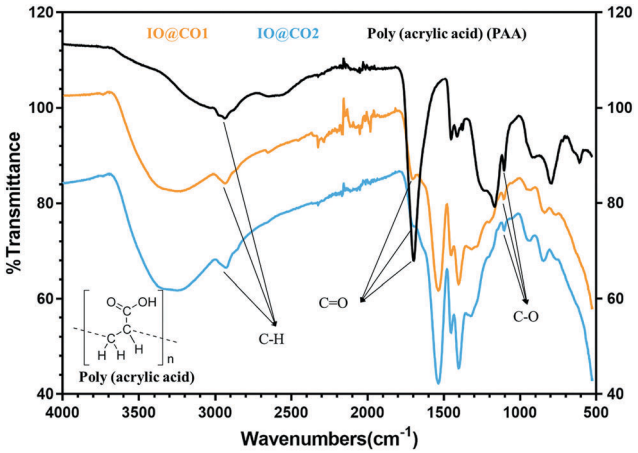

Fig. 3 Infrared spectra of IO@CO nanoparticles and PAA obtained using Fourier Transform Infrared (FTIR) spectroscopy. IO@CO1, IO@CO2 and PAA powders were dried, followed by FTIR measurement. Three strong peaks appearing at around 2800 cm^{-1} show the existence of carbon–hydrogen bonds. Three peaks near 1700 cm^{-1} indicate the existence of carbon–oxygen double bonds. Three weak peaks observed at 1150 cm^{-1} are carbon–oxygen bonds. According to the PAA structure and infrared spectroscopy, PAA was successfully coated on the nanoparticles.

the relaxation rate than IO@CO1, which could result from the thinner surrounding CeO_2 layer. However, both IO@CO1 and IO@CO2 are good contrast agents and can be used in further *in vitro* MRI studies.

ROS scavenging capability of IO@CO nanoparticles

Previous studies illustrated that cerium oxide nanoparticles have catalase mimetic activity, and were able to reduce the level of hydrogen peroxide H_2O_2.[39] Here, we investigated whether our IO@CO nanoparticles have ROS scavenging ability. We use the H_2O_2–HRP–ABTS system to test the anti-ROS capability of the nanoparticles. Briefly, ABTS (2,2′-azino-bis(3-ethylbenzothiazoline-6-sulphonic acid)) was oxidized by hydrogen peroxide (H_2O_2) in the presence of horseradish peroxidase (HRP) as a catalyst. As mentioned previously, cerium oxide can scavenge both H_2O_2 and superoxide radical when the cerium oxidation state changes between trivalent and tetravalent. Therefore, we incubated our nanoparticles with hydrogen peroxide followed by adding HRP. Finally, ABTS was added to detect ROS. We observed a significant decrease in the absorbance (directly proportional to the ROS level) when the concentration of cerium increased to 280 ng/100 μL and above (Fig. 6). Moreover, the nanoparticles with a Ce concentration of 1120 ng/100 μL were

A

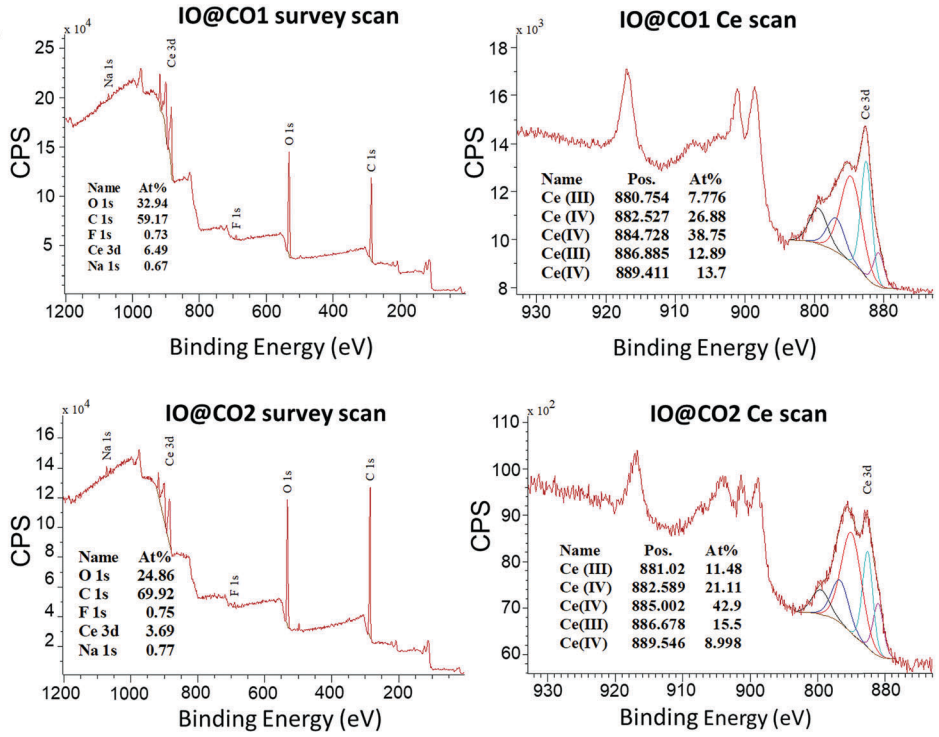

B

Sample	Ce^{3+}(At%)	Ce^{4+}(At%)	%Surface Ce^{3+}	%Surface Ce^{4+}	Ce^{3+} : Ce^{4+}
IO@CO1	1.2341	4.7383	20%	80%	1 : 4
IO@CO2	0.9399	2.5428	26.9%	73.1%	1 : 3

Fig. 4 X-ray photoelectron spectroscopy (XPS) of IO@CO nanoparticles. The Ce^{3+} : Ce^{4+} ratio is an important characteristic that is related to the antioxidant ability of the IO@CO nanoparticles. (A) The graph showing survey and Ce scans of IO@CO1 and IO@CO2. (B) Table showing the surface Ce^{3+}, Ce^{4+}, and Ce^{3+} : Ce^{4+} ratio of IO@CO1 and IO@CO2.

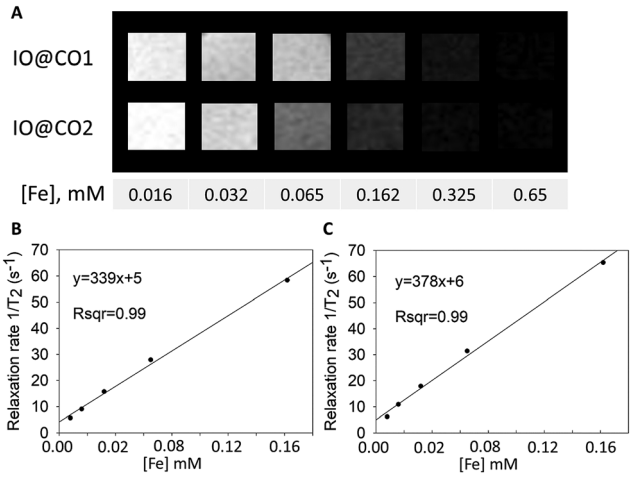

Fig. 5 MRI of IO@CO nanoparticle phantoms. (A) MRI images of IO@CO1 and IO@CO2 phantoms. IO@CO1 and IO@CO2 were diluted to different concentrations, followed by imaging using 9.4 T MRI. (B) Graph plotting the relationship of the relaxation rate and the iron concentration of IO@CO1. (C) Graph plotting the relationship of the relaxation rate and the iron concentration of IO@CO2.

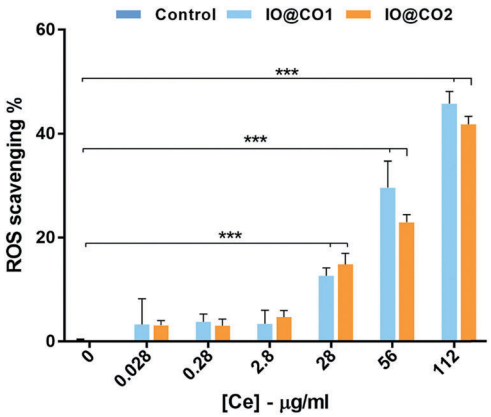

Fig. 6 ROS scavenging study of IO@CO nanoparticles. Different concentrations of the nanoparticles were treated with H_2O_2, followed by HRP treatment. Then ABTS was added into each reaction and absorbance was measured by Tecan X200. The absorbance of the 0 μg mL^{-1} sample was determined as 0% ROS scavenging. ***$P < 0.001$.

able to scavenge nearly half of the ROS in the solution. Our result showed that the IO@CO nanoparticles have anti-ROS ability in the buffer solution.

Nanoparticle uptake in macrophage J774A-1

Before conducting the *in vitro* cell-based studies, we sought to determine the macrophage uptake of these nanoparticles to make sure our nanoparticles can work inside the cells. Macrophages were used for our *in vitro* experiments as they are the cells responsible for ROS production under inflammatory conditions.[5,12] Macrophages were treated with the nanoparticles of different concentrations. The cells were washed and lysed, followed by measuring the cerium and iron concentrations in the cell lysis buffer.

The result of the ICP-MS measurement (Fig. 7) indicated that our nanoparticles exhibited good macrophage uptake. The results obtained from both cerium and iron uptake in the cells indicated that these IO@CO nanoparticles successfully entered into the macrophage cells with considerable quantity. When treated with higher concentrations of the nanoparticles, both cerium and iron uptake in macrophages significantly increased. The ratios of Ce to Fe uptaken by the cells were compared with the ratios of Ce to Fe in the nanoparticles (Fig. 7B). For IO@CO1, the ratios in the cells were detected lower than the ratio in the nanoparticles. For IO@CO2, the ratios in the cells were slightly less than the ratio in the nanoparticle. The decrease of the Ce/Fe ratio could be explained by the loss of cerium oxide in the IO@CO nanoparticles due to nanoparticle degradation at a low pH within the lysosome environment. Our degradation studies (Fig. S2, ESI†) showed that the size of the IO@CO nanoparticles slightly decreased at an acidic pH condition (pH 5.5). This could be explained by the shrinkage of poly(acrylic acid) in a low pH environment due to the protonation of carboxylic groups.[65] The reduced size of the nanoparticles could also be related to the dissolution of cerium oxide under acidic conditions.[66] The reason why IO@CO1 exhibited a larger decrease in the Ce/Fe ratio in the cell, compared to IO@CO2, is unclear but may be due to the higher loading of CeO_2 on IO@CO2, leading to a more pronounced change of Ce/Fe ratios when CeO_2 is degraded.

It was noted that the IO@CO nanoparticles are highly negatively charged (−55 mV) but able to be taken up by the cells. This can be explained as follows. Basically, the cell membranes should repulse the negatively charged IO@CO because of the large amount of negatively charged domains on their surface. However, Wilhelm *et al.*[60] indicated that with a repulsive force from the negatively charged domains on the surface of the membranes, the negatively charged nanoparticles will form into small groups then bind at the cationic sites on the surface. Meanwhile, the existing nanoparticles on the cell surface can reduce the density of the surface charge, which will benefit the adsorption of other nanoparticles. Therefore, the process of adsorption of the nanoparticles on the cell surface and the formation of the particle clusters are related to their cell uptake. Studies by Limbach *et al.* and Patil *et al.* on human lung cells also indicated that cells rapidly absorb negatively charged ceria nanoparticles.[61,62] In addition, Tabata *et al.* suggested that the lowest uptake of the nanoparticles in macrophages is related to the surface charge with a zeta potential of zero. In their study, negatively charged cell membranes along with the cations in the cell culture medium such as Ca^{2+} and Mg^{2+} were closely related to the cell uptake of both of their positively and negatively charged microspheres.[63]

In vitro magnetic resonance imaging of IO@CO nanoparticles in macrophages

In the last decades, SPIONs have been widely studied for imaging technology. For example, Cheng *et al.* indicated that aqueous dispersions of Fe_3O_4 nanoparticles exhibited excellent imaging ability in the cell with low cytotoxicity.[40] Ta *et al.* has developed different iron oxide nanoparticles for the molecular MR

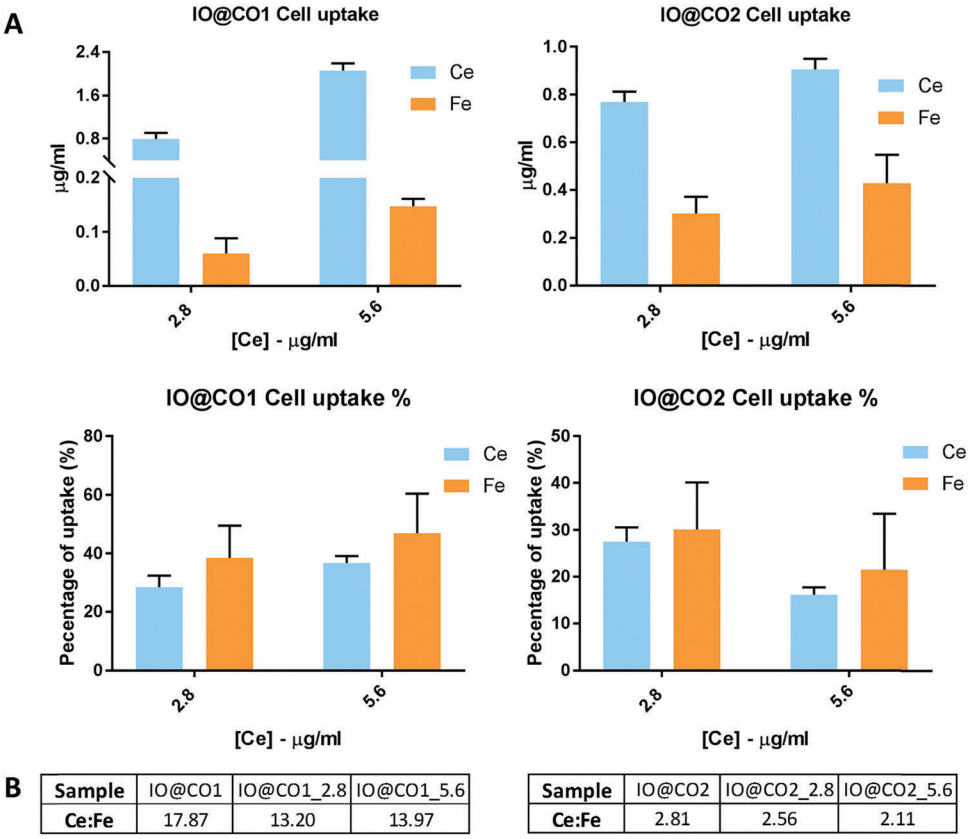

Sample	IO@CO1	IO@CO1_2.8	IO@CO1_5.6
Ce:Fe	17.87	13.20	13.97

Sample	IO@CO2	IO@CO2_2.8	IO@CO2_5.6
Ce:Fe	2.81	2.56	2.11

Fig. 7 Cell uptake of IO@CO nanoparticles as determined by ICP-MS. (A) Graphs showing the cell uptake of IO@CO. Macrophage cells were incubated with the IO@CO nanoparticles overnight. The cells were subsequently lysed. Iron and cerium concentrations were detected by ICP-MS. The graphs showed that both IO@CO1 and IO@CO2 were uptaken by macrophages. (B) Tables showing ratios of cerium to iron in the nanoparticle stocks and in cells.

imaging of cardiovascular diseases such as atherothrombosis.[41–46] After confirming that the IO@CO nanoparticles are good contrast agents, we investigated the contrast ability of the nanoparticles inside macrophage J774A.1. The cells were incubated for 24 h with the nanoparticles and subsequently fixed by paraformaldehyde. Then the cell pellet was embedded in a 0.5% agarose gel followed by MRI measurement.

The relaxation rates (Fig. 8A) and MR images (Fig. 8B) of the nanoparticle-treated cells showed a considerable enhancement compared to those without nanoparticles. Especially IO@CO2 exhibited a much stronger MRI T_2 effect and a higher relaxation rate than IO@CO1. The stronger T_2 contrast effect of IO@CO2 could result from its higher iron uptake as shown in the cell uptake study. These results showed that both IO@CO1 and IO@CO2 were able to image macrophage cells; especially IO@CO2 exhibited a more significant imaging contrast effect.

Biocompatibility of IO@CO nanoparticles

Before testing the ROS quenching ability of the IO@CO nanoparticles in the cells, it is necessary to investigate the cytotoxic effect of these nanoparticles, even though it was reported that cerium oxide nanoparticles exhibited no toxic effect on macrophage cells.[49] Macrophages J774A.1 (20 000 cells per well) were used to test the cytotoxic effect of the nanoparticles and were treated with different concentrations of nanoparticles for 24 hours and 48 hours. The cells were then washed and subsequently treated with EthD-1 that marked the dead macrophage nucleus and can be detected by its red fluorescence. The cells were imaged using fluorescence microscopy (Fig. 9B) and the fluorescence intensity was measured using a plate reader (Fig. 9A). There was no significant difference between the live cell control and nanoparticle-treated groups. Fluorescence images also indicated a low cytotoxicity of the nanoparticles after 24-hour treatment. In two-day treatment, macrophages treated with IO@CO2 still showed very good cell viability. However, we observed a slight decrease in the viability of macrophages treated with high concentrations of IO@CO1. The result indicated that IO@CO1 exhibited some toxic effects on macrophage cells, while IO@CO2 exhibited no cytotoxic effect in any concentrations and time periods tested in the study.

In vitro cell-based assay of ROS scavenging capability

Reactive oxygen species have been related to a broad spectrum of inflammatory diseases such as atherosclerosis and rheumatoid arthritis. In this decade, cerium oxide nanoparticles have been confidently shown to have the ROS scavenging capability *in vitro*.

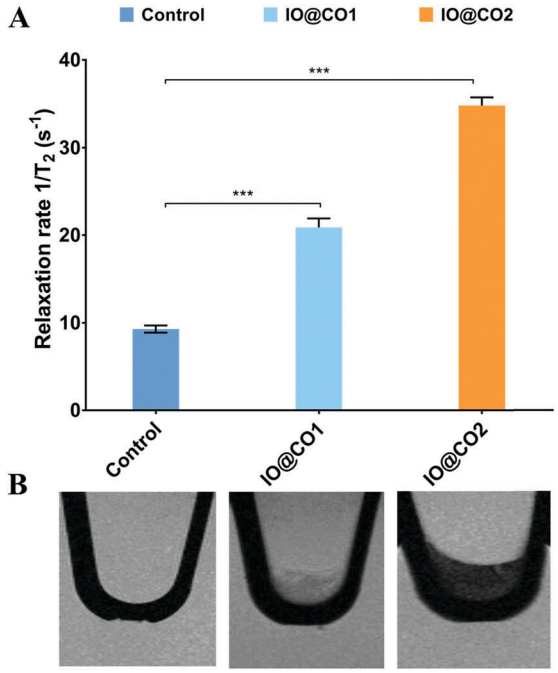

Fig. 8 *In vitro* MRI of IO@CO nanoparticles. Macrophage cells were incubated with the IO@CO nanoparticles overnight. The cells were subsequently fixed, suspended in a 0.5% agarose gel and imaged by MRI. (A) Graph showing the relaxation rate of the non-treated cells, and cells treated with IO@CO1 and IO@CO2. The relaxation rate of the nanoparticle-treated sample is higher than that of the non-treated group (Control). (B) MRI images of the cells. Both CO@IO1 and CO@IO2 nanoparticle-treated samples exhibited a significant imaging signal (dark color) compared to the non-treated group (control). In addition, the cells incubated with IO@CO2 exhibited a stronger negative MRI effect than the cells incubated with IO@CO1. ***$P < 0.001$.

Schubert *et al.* in 2006 firstly showed that cerium oxide nanoparticles (with a $Ce^{3+}:Ce^{4+}$ ratio of 3 : 47) can protect rat hippocampal nerve cells from hydrogen peroxide-induced cell death effectively[50] and it also worked on human breast fibrosarcoma cells.[51] In addition, in 2009 Hirst *et al.* showed cerium oxide nanoparticles can reduce ROS in macrophage J774A.1 cells significantly.[49]

In our studies, we chose to use macrophage as our cell model as it has been reported as a major factor in many inflammatory diseases.[52–54] Due to the higher toxicity of IO@CO1, IO@CO2 was chosen for *in vitro* cell-based assay of the ROS scavenging effect. Macrophages were incubated for 24 hours with different concentrations of nanoparticles and subsequently stimulated with 1.5 mM H_2O_2. After that, dichlorofluorescin diacetate (DCF_DA) was used to detect the ROS levels in the cells. H_2O_2 is the most studied and best-characterized member of ROS and it can be considered as the most important ROS in redox signaling. The fluorescence intensity (Fig. 10A) showed that compared to the H_2O_2 treated control group, the ROS level of the cells treated with 0.056 μg Ce/mL was significantly decreased. When the Ce concentration increases to 0.14 μg mL^{-1} and above, the ROS level of the treated cells was lowered to the ROS level of the control non-stimulated cells. The fluorescence images (Fig. 10B) of the nanoparticle-treated macrophages showed a similar fluorescence signal to the non-stimulated cell control group and significantly weaker than the stimulated cell control group. These results confirmed the ROS scavenging ability of our IO@CO2 *in vitro*.

Atherosclerosis, rheumatoid arthritis, allergies and other autoimmune diseases are basically caused by chronic inflammation, which is related to the disorder of inflammatory regulation or switching off.[5] These inflammatory disorders have a strong relationship with the high level of ROS in the lesions.[6,55] For example, atherosclerosis, taking the largest proportion in the CVDs, is a complex disease that happens in the intima of arteries and can be progressive for many years.[14] In the progression of atherosclerosis, ROS play an important role in the oxidation of low-density lipoprotein in the intima of the blood vessel by macrophages.[56] The high level of the ROS along with the cytokines released by the dead macrophage attracts more macrophage to accumulate into the atherosclerosis plaque, making the situation worse.[48] Similarly, in many joint diseases, ROS and NO along with some pro-inflammatory factors such as prostaglandins and cytokines are produced at the sites of inflammation and are responsible for the progression of the diseases.[57]

Our result (Fig. 6) showed that IO@CO exhibited good anti-ROS ability in the buffer solution. *In vitro* cell-based ROS scavenging results (Fig. 10) indicated that IO@CO2 could reduce the ROS level in macrophage cells, implying that this nanoparticle can be a potential treatment agent for inflammatory diseases such as cardiovascular disease and rheumatoid arthritis. The anti-ROS capability could be due to the regenerative antioxidant properties from cerium oxide.[58] When the trivalent cerium ions change to tetravalent cerium ions, cerium ions are capable of scavenging superoxide radical. In contrast, when it comes back from tetravalent cerium ions to trivalent cerium ions, cerium ions show the ability of scavenging H_2O_2. These regenerative antioxidant capabilities are the major reasons that the IO@CO nanoparticles can reduce the ROS level in macrophage cells. Dowding *et al.* recently showed that changing of the $Ce^{3+}:Ce^{4+}$ ratio on the nanoparticle surface can alter the biological interactions of the nanoparticle.[59] In addition, it is shown that 22% of the Ce^{3+} ion on the surface of the nanoparticles will significantly contribute the stronger activities of superoxide dismutase.[19] In our study, the reliable antioxidant activity of the IO@CO nanoparticles owes to the ideal concentration of the Ce^{3+} ion (20% and 26.9%) on their surface, which contributes to the good ROS scavenging ability of these IO@CO nanoparticles. In Bae *et al.*'s study,[67] they developed hydrogen peroxide-responsive antioxidant copolyoxalates containing hydroxybenzyl alcohol (HPOX) and vanillyl alcohol (PVAX) nanoparticles, which showed a good H_2O_2 scavenging ability of around 40% to 60% after 24 hours treatment with 1 mg mL^{-1} of their nanoparticles. IO@CO exhibits a good anti-H_2O_2 ability at 50% after only 1 hour treatment with just 112 μg mL^{-1} of cerium oxide of IO@CO. In the *in vitro* cell study, IO@CO2 showed more than 50% scavenging of ROS at 0.14 μg mL^{-1} and 1.4 μg mL^{-1} of cerium oxide of IO@CO2. In Liu *et al.*'s[68] study, the ROS scavenging ability of 1 μM nano-CeO_2 (12 h treatment)

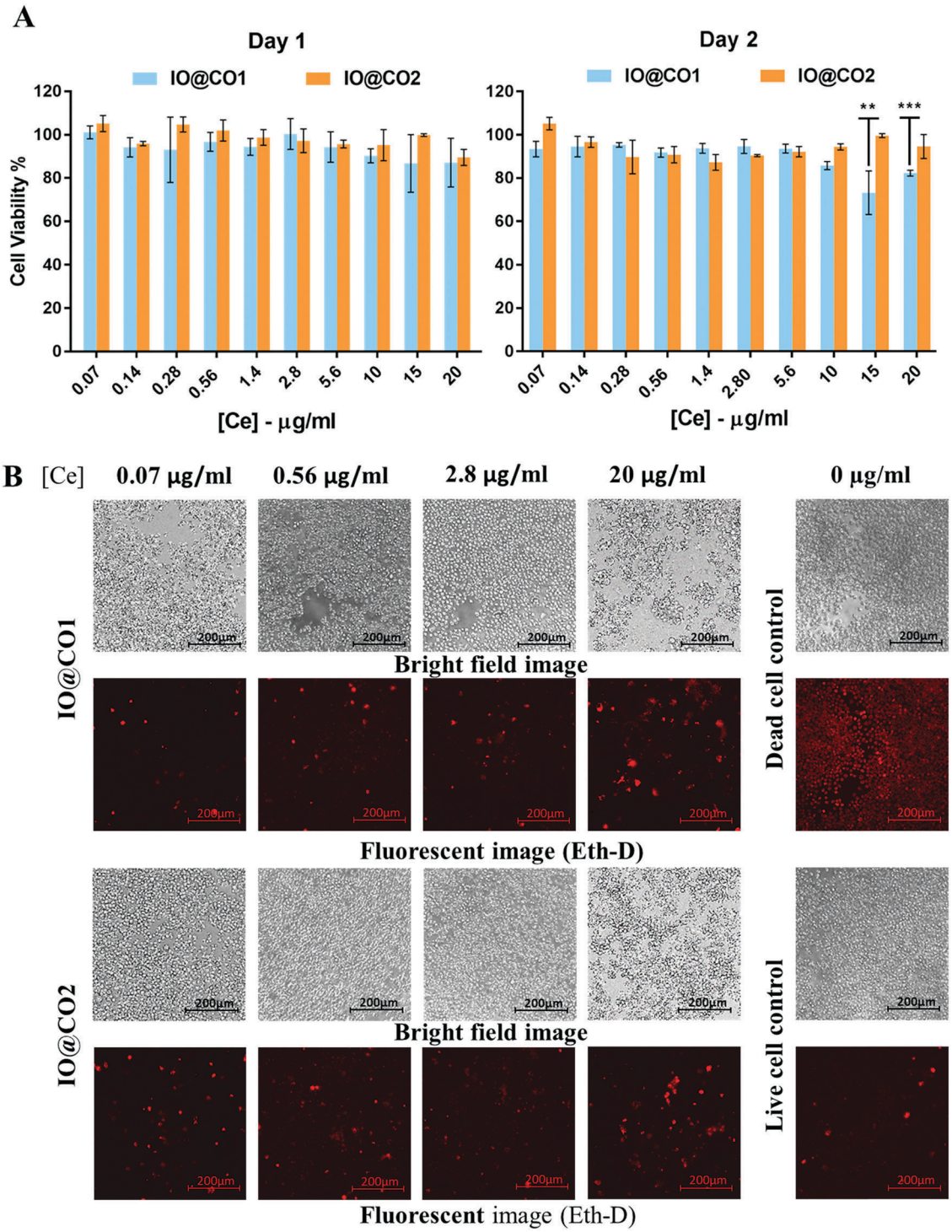

Fig. 9 Viability/toxicity study of macrophage cells with nanoparticles. Macrophage cells were incubated with IO@CO nanoparticles for one or two days. Dead cells were stained with EthD-1 and showed the red fluorescence under fluorescence microscopy. The fluorescence intensity was measured by Tecan X200. (A) Graph showing the viability of the cells after one- or two-day incubation with the nanoparticles. It showed that the cell viability was around 90–100% for all different concentrations of the nanoparticles, except the cells that were treated with IO@CO1 in very high concentrations. These cells showed approximately 70–80% of cell viability. (B) Fluorescence images of the cells taken on the first day of the nanoparticle treatment. It showed that the toxicity of the IO@CO nanoparticles was acceptable. $^{**}P < 0.01$, $^{***}P < 0.001$.

was around 20% in HepG2 cells that were exposed to 0.6 mM H_2O_2 for 12 hours. In our study, macrophage J774.A1 was treated with IO@CO2 for 24 hours, followed by 1 hour incubation with 1.5 mM H_2O_2. It showed a good ROS scavenging of around 73% when the cerium concentration of IO@CO2 was 0.14 µg mL^{-1}.

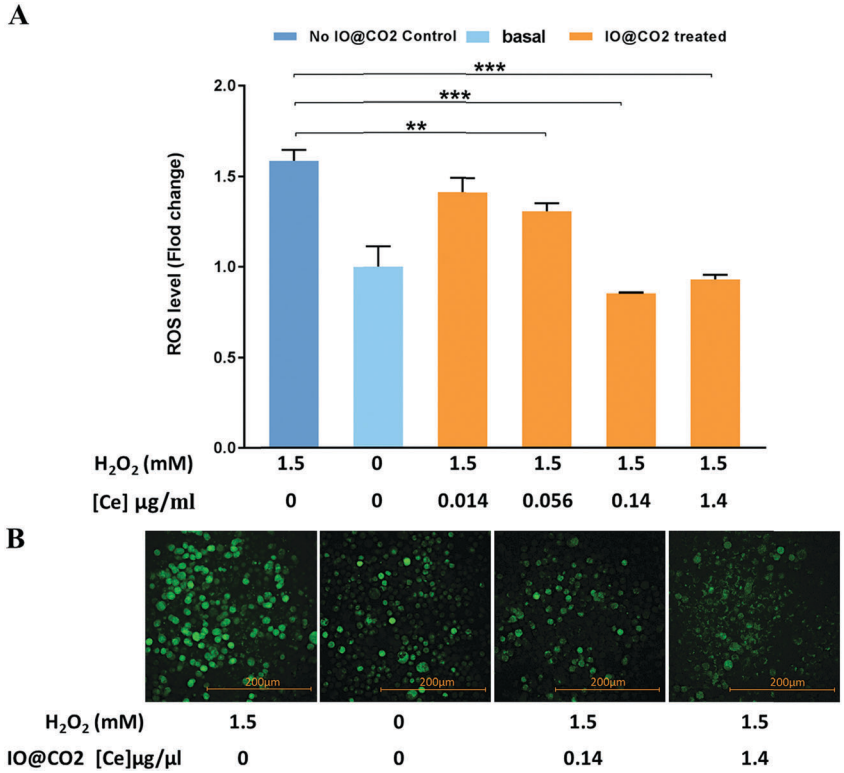

Fig. 10 ROS scavenging ability of IO@CO nanoparticles in macrophage cells. Macrophage cells were incubated with IO@CO nanoparticles overnight, followed by stimulation with H_2O_2. ROS inside the cells were detected by DCF_DA. The fluorescence intensity was measured by Tecan X200 and fluorescence images were taken using fluorescence microscopy. (A) Graph showing the ROS level of the cells. Cells treated with a low concentration of the nanoparticles showed a significant reduction of ROS when the concentration of cerium reached 14 ng/100 µL and above. (B) Fluorescence images of the cells. The images showed that cells treated with different concentrations of nanoparticles and H_2O_2 exhibited a significantly lower green fluorescence signal than the cells treated with H_2O_2. $^{**}P < 0.01$, $^{***}P < 0.001$.

Conclusions

The presented work demonstrates a successful synthesis of iron oxide/cerium oxide core–shell (IO@CO) nanoparticles. The IO@CO nanoparticles were shown to be a good contrast agent under MRI, and they also exhibited a good $Ce^{3+}:Ce^{4+}$ ratio. *In vitro* studies showed that our nanoparticles exhibited good cell uptake, strong cell MRI, low cell cytotoxicity and good ROS scavenging ability. The results showed that the IO@CO nanoparticle could decrease the ROS level in the stimulated J774A.1 macrophages. The ROS scavenging ability of IO@CO in macrophages makes this nanoparticle a potential treatment agent for ROS-related inflammatory diseases such as atherosclerosis and rheumatoid arthritis. In addition, good MRI imaging capability of the nanoparticle indicates its potential use for detecting and monitoring the treatment of inflammatory diseases. In conclusion, the IO@CO nanoparticles can be a potential theranostic agent for inflammatory diseases. In the future, we will conjugate our nanoparticle with antibodies or binding peptides to target inflammatory markers. For example, vascular cell adhesion molecule 1 (VCAM-1) is one of the important adhesion molecules secreted by the inflamed endothelial cells especially those in atherosclerotic plaques.[47] Therefore, VCAM-1 is an effective biomarker to detect endothelial inflammation, improving the progress for both early phase treatment and early stage detection of atherosclerosis and CVD. In rheumatoid arthritis, neutrophil cytosolic factor 1 can be a good biomarker of RA as it is highly expressed in the position of the inflammation of the rheumatoid arthritis patients.[48] By employing effective targeting ligands, these nanoparticles can detect the early stage of atherosclerosis, rheumatoid arthritis and other ROS related inflammatory diseases. In addition, further studies on the applications of these nanoparticles in animal models of inflammatory diseases will be conducted in the future.

Conflicts of interest

Nothing to declare.

Acknowledgements

This work received financial support from the Australian National Health and Medical research council (H. T. T: APP1037310, APP1146694) and the Australian research council (R. Z, A. K. W: CE140100036). The authors would like to acknowledge the Australian National Fabrication Facility (Queensland Node); the National Imaging Facility, Centre for Advanced Imaging for access to key items of equipment. The authors gratefully thank all the colleagues in the Australian Institute for Bioengineering and Nanotechnology for their comments and help.

References

1 S. Barquera, A. Pedroza-Tobias, C. Medina, L. Hernandez-Barrera, K. Bibbins-Domingo, R. Lozano and A. E. Moran, *Arch. Med. Res.*, 2015, **46**, 328–338.

2 M. Naghavi, H. D. Wang, R. Lozano, A. Davis, X. F. Liang, M. G. Zhou, S. E. Vollset, A. A. Ozgoren, S. Abdalla, F. Abd-Allah, M. I. A. Aziz, S. F. Abera, V. Aboyans, B. Abraham, J. P. Abraham, K. E. Abuabara, I. Abubakar, L. J. Abu-Raddad, N. M. E. Abu-Rmeileh, T. Achoki, A. Adelekan, Z. N. Ademi, K. Adofo, A. K. Adou, J. C. Adsuar, J. Aernlov, E. E. Agardh, D. Akena, M. J. Al Khabouri, D. Alasfoor, M. Albittar, M. A. Alegretti, A. V. Aleman, Z. A. Alemu, R. Alfonso-Cristancho, S. Alhabib, M. K. Ali, R. Ali, F. Alla, F. Al Lami, P. Allebeck, M. A. AlMazroa, R. A. S. Salman, U. Alsharif, E. Alvarez, N. Alviz-Guzman, A. A. Amankwaa, A. T. Amare, O. Ameli, H. Amini, W. Ammar, H. R. Anderson, B. O. Anderson, C. A. T. Antonio, P. Anwari, H. Apfel, S. A. Cunningham, V. S. A. Arsenijevic, A. Artaman, M. M. Asad, R. J. Asghar, R. Assadi, L. S. Atkins, C. Atkinson, A. Badawi, M. C. Bahit, T. Bakfalouni, K. Balakrishnan, S. Balalla, A. Banerjee, R. M. Barber, S. L. Barker-Collo, S. Barquera, L. Barregard, L. H. Barrero, T. Barrientos-Gutierrez, A. Basu, S. Basu, M. O. Basulaiman, J. Beardsley, N. Bedi, E. Beghi, T. Bekele, M. L. Bell, C. Benjet, D. A. Bennett, I. M. Bensenor, H. Benzian, A. Bertozzi-Villa, T. J. Beyene, N. Bhala, A. Bhalla, Z. A. Bhutta, B. Bikbov, A. Bin Abdulhak, S. Biryukov, J. D. Blore, F. M. Blyth, M. A. Bohensky, G. Borges, D. Bose, S. Boufous, R. R. Bourne, L. N. Boyers, M. Brainin, M. Brauer, C. E. G. Brayne, A. Brazinova, N. Breitborde, H. Brenner, A. D. M. Briggs, J. C. Brown, T. S. Brugha, G. C. Buckle, L. N. Bui, G. Bukhman, M. Burch, I. R. C. Nonato, H. Carabin, R. Cardenas, J. Carapetis, D. O. Carpenter, V. Caso, C. A. Castaneda-Orjuela, R. E. Castro, F. Catala-Lopez, F. Cavalleri, J. C. Chang, F. C. Charlson, X. Che, H. L. Chen, Y. Y. Chen, J. S. Chen, Z. M. Chen, P. P. C. Chiang, O. Chimed-Ochir, R. Chowdhury, H. Christensen, C. A. Christophi, T. W. Chuang, S. S. Chugh, M. Cirillo, M. M. Coates, L. E. Coffeng, M. S. Coggeshall, A. Cohen, V. Colistro, S. M. Colquhoun, M. Colomar, L. T. Cooper, C. Cooper, L. M. Coppola, M. Cortinovis, K. Courville, B. C. Cowie, M. H. Criqui, J. A. Crump, L. Cuevas-Nasu, I. D. C. Leite, K. C. Dabhadkar, L. Dandona, R. Dandona, E. Dansereau, P. I. Dargan, A. Dayama, V. De la Cruz-Gongora, S. F. de la Vega, D. De Leo, L. Degenhardt, B. del Pozo-Cruz, R. P. Dellavalle, K. Deribe, D. C. D. Jarlais, M. Dessalegn, G. A. deVeber, S. D. Dharmaratne, M. Dherani, J. L. Diaz-Ortega, C. Diaz-Torne, D. Dicker, E. L. Ding, K. Dokova, E. R. Dorsey, T. R. Driscoll, L. L. Duan, H. C. Duber, A. M. Durrani, B. E. Ebel, K. M. Edmond, R. G. Ellenbogen, Y. Elshrek, S. P. Ermakov, H. E. Erskine, B. Eshrati, A. Esteghamati, K. Estep, T. Furst, S. Fahimi, A. S. Fahrion, E. J. A. Faraon, F. Farzadfar, D. F. J. Fay, A. B. Feigl, V. L. Feigin, M. M. Felicio, S. M. Fereshtehnejad, J. G. Fernandes, A. J. Ferrari, T. D. Fleming, N. Foigt, K. Foreman, M. H. Forouzanfar, F. G. R. Fowkes, U. F. Paleo, R. C. Franklin, N. D. Futran, L. Gaffikin, K. Gambashidze, F. G. Gankpe, F. A. Garcia-Guerra, A. C. Garcia, J. M. Geleijnse, B. D. Gessner, K. B. Gibney, R. F. Gillum, S. Gilmour, I. Abdelmageem, M. Ginawi, M. Giroud, E. L. Glaser, S. Goenka, H. G. Dantes, P. Gona, D. Gonzalez-Medina, C. Guinovart, R. Gupta, R. Gupta, R. A. Gosselin, C. C. Gotay, A. Goto, H. N. Gowda, N. Graetz, K. F. Greenwell, H. C. Gugnani, D. Gunnell, R. A. Gutierrez, J. Haagsma, N. Hafezi-Nejad, H. Hagan, M. Hagstromer, Y. A. Halasa, R. R. Hamadeh, H. Hamavid, M. Hammami, J. Hancock, G. J. Hankey, G. M. Hansen, H. L. Harb, H. Harewood, J. M. Haro, R. Havmoeller, R. J. Hay, S. I. Hay, M. T. Hedayati, I. B. H. Pi, K. R. Heuton, P. Heydarpour, H. Higashi, M. Hijar, H. W. Hoek, H. J. Hoffman, J. C. Hornberger, H. D. Hosgood, M. Hossain, P. J. Hotez, D. G. Hoy, M. Hsairi, G. Q. Hu, J. J. Huang, M. D. Huffman, A. J. Hughes, A. Husseini, C. Huynh, M. Iannarone, K. M. Iburg, B. T. Idrisov, N. Ikeda, K. Innos, M. Inoue, F. Islami, S. Ismayilova, K. H. Jacobsen, S. Jassal, S. P. Jayaraman, P. N. Jensen, V. Jha, G. H. Jiang, Y. Jiang, J. B. Jonas, J. Joseph, K. Juel, E. K. Kabagambe, H. D. Kan, A. Karch, C. Karimkhani, G. Karthikeyan, N. Kassebaum, A. Kaul, N. Kawakami, K. Kazanjan, D. S. Kazi, A. H. Kemp, A. P. Kengne, A. Keren, M. Kereselidze, Y. S. Khader, S. E. A. H. Khalifa, E. A. Khan, G. Khan, Y. H. Khang, C. Kieling, Y. Kinfu, J. M. Kinge, D. Kim, S. Kim, M. Kivipelto, L. Knibbs, A. K. Knudsen, Y. Kokubo, S. Kosen, M. Kotagal, M. A. Kravchenko, S. Krishnaswami, H. Krueger, B. K. Defo, E. J. Kuipers, B. K. Bicer, C. Kulkarni, V. S. Kulkarni, K. Kumar, R. B. Kumar, G. F. Kwan, H. Kyu, T. Lai, A. L. Balaji, R. Lalloo, T. Lallukka, H. Lam, Q. Lan, V. C. Lansingh, H. J. Larson, A. Larsson, P. M. Lavados, A. E. B. Lawrynowicz, J. L. Leasher, J. T. Lee, J. Leigh, M. Leinsalu, R. Leung, C. Levitz, B. Li, Y. C. Li, Y. M. Li, C. Liddell, S. S. Lim, G. M. F. de Lima, M. L. Lind, S. E. Lipshultz, S. W. Liu, Y. Liu, B. K. Lloyd, K. T. Lofgren, G. Logroscino, S. J. London, J. Lortet-Tieulent, P. A. Lotufo, R. M. Lucas, R. Lunevicius, R. A. Lyons, S. Ma, V. M. P. Machado, M. F. MacIntyre, M. T. Mackay, J. H. MacLachlan, C. Magis-Rodriguez, A. A. Mahdi, M. Majdan, R. Malekzadeh, S. Mangalam, C. C. Mapoma, M. Marape, W. Marcenes, C. Margono, G. B. Marks, M. B. Marzan, J. R. Masci, M. T. Q. Mashal, F. Masiye, A. J. Mason-Jones, R. Matzopolous, B. M. Mayosi, T. T. Mazorodze, J. J. McGrath, A. C. Mckay, M. Mckee, A. McLain, P. A. Meaney, M. M. Mehndiratta, F. Mejia-Rodriguez, Y. A. Melaku, M. Meltzer, Z. A. Memish, W. Mendoza, G. A. Mensah, A. Meretoja, F. A. Mhimbira, T. R. Miller, E. J. Mills, A. Misganaw, S. K. Mishra, C. N. Mock, T. E. Moffitt, N. M. Ibrahim, K. A. Mohammad, A. H. Mokdad, G. L. Mola, L. Monasta, J. D. Monis, J. C. M. Hernandez, M. Montico, T. J. Montine, M. D. Mooney, A. R. Moore, M. Moradi-Lakeh, A. E. Moran, R. Mori, J. Moschandreas, W. N. Moturi, M. L. Moyer,

D. Mozaffarian, U. O. Mueller, M. Mukaigawara, E. C. Mullany, J. Murray, A. Mustapha, P. Naghavi, A. Naheed, K. S. Naidoo, L. Naldi, D. Nand, V. Nangia, K. M. V. Narayan, D. Nash, J. Nasher, C. Nejjari, R. G. Nelson, M. Neuhouser, S. P. Neupane, P. A. Newcomb, L. Newman, C. R. Newton, M. Ng, F. N. Ngalesoni, G. Nguyen, N. T. T. Nguyen, M. I. Nisar, S. Nolte, O. F. Norheim, R. E. Norman, B. Norrving, L. Nyakarahuka, S. Odell, M. O'Donnell, T. Ohkubo, S. L. Ohno, B. O. Olusanya, S. B. Omer, J. N. Opio, O. E. Orisakwe, K. F. Ortblad, A. Ortiz, M. L. K. Otayza, A. W. Pain, J. D. Pandian, C. I. Panelo, J. Panniyammakal, C. Papachristou, A. J. P. Caicedo, S. B. Patten, G. C. Patton, V. K. Paul, B. Pavlin, N. Pearce, C. A. Pellegrini, D. M. Pereira, S. C. Peresson, R. Perez-Padilla, F. P. Perez-Ruiz, N. Perico, A. Pervaiz, K. Pesudovs, C. B. Peterson, M. Petzold, B. K. Phillips, D. E. Phillips, M. R. Phillips, D. Plass, F. B. Piel, D. Poenaru, S. Polinder, S. Popova, R. G. Poulton, F. Pourmalek, D. Prabhakaran, D. Qato, A. D. Quezada, D. A. Quistberg, F. Rabito, A. Rafay, K. Rahimi, V. Rahimi-Movaghar, S. U. R. Rahman, M. Raju, I. Rakovac, S. M. Rana, A. Refaat, G. Remuzzi, A. L. Ribeiro, S. Ricci, P. M. Riccio, L. Richardson, J. H. Richardus, B. Roberts, D. A. Roberts, M. Robinson, A. Roca, A. Rodriguez, D. Rojas-Rueda, L. Ronfani, R. Room, G. A. Roth, D. Rothenbacher, D. H. Rothstein, J. T. Rowley, N. Roy, G. M. Ruhago, L. Rushton, S. Sambandam, K. Soreide, M. Y. Saeedi, S. Saha, R. Sahathevan, M. A. Sahraian, B. W. Sahle, J. A. Salomon, D. Salvo, G. M. J. Samonte, U. Sampson, J. R. Sanabria, L. Sandar, I. S. Santos, M. Satpathy, M. Sawhney, M. Saylan, P. Scarborough, B. Schottker, J. C. Schmidt, I. J. C. Schneider, A. E. Schumacher, D. C. Schwebel, J. G. Scott, S. G. Sepanlou, E. E. Servan-Mori, K. Shackelford, A. Shaheen, S. Shahraz, M. Shakh-Nazarova, S. Shangguan, J. She, S. Sheikhbahaei, D. S. Shepard, K. Shibuya, Y. Shinohara, K. Shishani, I. Shiue, R. Shivakoti, M. G. Shrime, I. D. Sigfusdottir, D. H. Silberberg, A. P. Silva, E. P. Simard, S. Sindi, J. A. Singh, L. Singh, E. Sioson, V. Skirbekk, K. Sliwa, S. So, M. Soljak, S. Soneji, S. S. Soshnikov, L. A. Sposato, C. T. Sreeramareddy, J. R. D. Stanaway, V. K. Stathopoulou, K. Steenland, C. Stein, C. Steiner, A. Stevens, H. Stoeckl, K. Straif, K. Stroumpoulis, L. Sturua, B. F. Sunguya, S. Swaminathan, M. Swaroop, B. L. Sykes, K. M. Tabb, K. Takahashi, R. T. Talongwa, F. Tan, D. Tanne, M. Tanner, M. Tavakkoli, B. T. Ao, C. M. Teixeira, T. Templin, E. Y. Tenkorang, A. S. Terkawi, B. A. Thomas, A. L. Thorne-Lyman, A. G. Thrift, G. D. Thurston, T. Tillmann, D. L. Tirschwell, I. M. Tleyjeh, M. Tonelli, F. Topouzis, J. A. Towbin, H. Toyoshima, J. Traebert, B. X. Tran, T. Truelsen, U. Trujillo, M. Trillini, Z. T. Dimbuene, M. Tsilimbaris, E. M. Tuzcu, C. Ubeda, U. S. Uchendu, K. N. Ukwaja, E. A. Undurraga, A. J. Vallely, S. van de Vijver, C. H. van Gool, Y. Y. Varakin, T. J. Vasankari, A. M. N. Vasconcelos, M. S. Vavilala, N. Venketasubramanian, L. Vijayakumar, S. Villalpando, F. S. Violante, V. V. Vlassov, G. R. Wagner, S. G. Waller, J. L. Wang, L. Wang, X. R. Wang, Y. P. Wang, T. S. Warouw, S. Weichenthal, E. Weiderpass, R. G. Weintraub, W. Wenzhi, A. Werdecker, K. R. R. Wessells, R. Westerman, H. A. Whiteford, J. D. Wilkinson, T. N. Williams, S. M. Woldeyohannes, C. D. A. Wolfe, T. M. Wolock, A. D. Woolf, J. Q. Wong, J. L. Wright, S. Wulf, B. Wurtz, G. L. Xu, Y. C. Yang, Y. Yano, H. Yatsuya, P. Yip, N. Yonemoto, S. J. Yoon, M. Younis, C. H. Yu, K. Y. Jin, M. E. S. Zaki, M. F. Zamakhshary, H. Zeeb, Y. Zhang, Y. Zhao, Y. F. Zheng, J. Zhu, S. Zhu, D. Zonies, X. N. Zou, J. R. Zunt, T. Vos, A. D. Lopez, C. J. L. Murray and G. M. C. D. Colla, *Lancet*, 2015, **385**, 117–171.

3 World Health Organization, Chronic rheumatic conditions, http://www.who.int/chp/topics/rheumatic/en/.

4 J. D. Lambeth, K. H. Krause and R. A. Clark, *Semin. Immunopathol.*, 2008, **30**, 339–363.

5 M. Mittal, M. R. Siddiqui, K. Tran, S. P. Reddy and A. B. Malik, *Antioxid. Redox Signaling*, 2014, **20**, 1126–1167.

6 C. A. Hitchon and H. S. El-Gabalawy, *Arthritis Res. Ther.*, 2004, **6**, 265–278.

7 X. F. Chen, M. J. Song, B. Zhang and Y. Zhang, *Oxid. Med. Cell. Longevity*, 2016, 1580967, DOI: 10.1155/2016/1580967.

8 S. Kossmann, M. Knorr, J. Stratmann, M. Hausding, S. Schuhmacher, S. H. Karbach, M. Schwenk, N. Vogev, E. Schulz, M. Oelze, S. Grabbe, H. Jonuleit, C. Becker, A. Daiber, A. Waisman, T. Munzel and P. Wenzel, *Vasc. Pharmacol.*, 2012, **56**, 317.

9 X. Y. Li, P. Fang, J. T. Mai, E. T. Choi, H. Wang and X. F. Yang, *J. Hematol. Oncol.*, 2013, **6**, 19.

10 J. D. Lambeth, *Nat. Rev. Immunol.*, 2004, **4**, 181–189.

11 N. H. Kim, S. Choi, E. J. Han, B. K. Hong, S. Y. Choi, H. M. Kwon, S. Y. Hwang, C. S. Cho and W. U. Kim, *Eur. J. Immunol.*, 2014, **44**, 2721–2736.

12 Y. A. Komarova, K. Kruse, D. Mehta and A. B. Malik, *Circ. Res.*, 2017, **120**, 179–206.

13 D. Mehta and A. B. Malik, *Physiol. Rev.*, 2006, **86**, 279–367.

14 J. L. Aldons, *Nature*, 2000, **407**, 233.

15 R. Ross, *Am. Heart J.*, 1999, **138**, S419–S420.

16 T. S. Hiran, P. J. Moulton and J. T. Hancock, *Free Radical Biol. Med.*, 1997, **23**, 736–743.

17 P. J. Moulton, T. S. Hiran, M. B. Goldring and J. T. Hancock, *Br. J. Rheumatol.*, 1997, **36**, 522–529.

18 M. A. Jakupec, P. Unfried and B. K. Keppler, *Rev. Physiol., Biochem. Pharmacol.*, 2005, **153**, 101–111.

19 C. Korsvik, S. Patil, S. Seal and W. T. Self, *Chem. Commun.*, 2007, 1056–1058, DOI: 10.1039/b615134e.

20 E. G. Heckert, S. Seal and W. T. Self, *Environ. Sci. Technol.*, 2008, **42**, 5014–5019.

21 S. Das, J. M. Dowding, K. E. Klump, J. F. McGinnis, W. Self and S. Seal, *Nanomedicine*, 2013, **8**, 1483–1508.

22 A. Karakoti, S. Singh, J. M. Dowding, S. Seal and W. T. Self, *Chem. Soc. Rev.*, 2010, **39**, 4422–4432.

23 M. Mahmoudi, S. Sant, B. Wang, S. Laurent and T. Sen, *Adv. Drug Delivery Rev.*, 2011, **63**, 24–46.

24 S. A. Wahajuddin, *Int. J. Nanomed.*, 2012, **7**, 3445–3471.

25 F. M. McQueen, *Rheumatology*, 2000, **39**, 700–706.

26 M. Back and G. K. Hansson, *Nat. Rev. Cardiol.*, 2015, **12**, 199–211.
27 F. Chen, E. B. Ehlerding and W. Cai, *J. Nucl. Med.*, 2014, **55**, 1919–1922.
28 D. Wang, B. B. Lin and H. Ai, *Pharm. Res.*, 2014, **31**, 1390–1406.
29 P. Couvreur, *Adv. Drug Delivery Rev.*, 2013, **65**, 21–23.
30 S. Ganta, H. Devalapally, A. Shahiwala and M. Amiji, *J. Controlled Release*, 2008, **126**, 187–204.
31 J. Park, K. J. An, Y. S. Hwang, J. G. Park, H. J. Noh, J. Y. Kim, J. H. Park, N. M. Hwang and T. Hyeon, *Nat. Mater.*, 2004, **3**, 891–895.
32 S. Sun and H. Zeng, *J. Am. Chem. Soc.*, 2002, **124**, 8204–8205.
33 T. Zhou, B. Y. Wu and D. Xing, *J. Mater. Chem.*, 2012, **22**, 470–477.
34 L. L. Pang, J. S. Li, J. H. Jiang, Y. Le, G. L. Shen and R. Q. Yu, *Sens. Actuators, B*, 2007, **127**, 311–316.
35 X. Wang, T. Yang and K. Jiao, *Biosens. Bioelectron.*, 2009, **25**, 668–673.
36 C. M. Yeung, K. M. Yu, Q. J. Fu, D. Thompsett, M. I. Petch and S. C. Tsang, *J. Am. Chem. Soc.*, 2005, **127**, 18010–18011.
37 F. F. Zhu, G. Z. Chen, S. X. Sun and X. Sun, *J. Mater. Chem. A*, 2013, **1**, 288–294.
38 T. Sugama, L. E. Kukacka and N. Carciello, *J. Mater. Sci.*, 1984, **19**, 4045–4056.
39 T. Pirmohamed, J. M. Dowding, S. Singh, B. Wasserman, E. Heckert, A. S. Karakoti, J. E. S. King, S. Seal and W. T. Self, *Chem. Commun.*, 2010, **46**, 2736–2738.
40 F. Y. Cheng, C. H. Su, Y. S. Yang, C. S. Yeh, C. Y. Tsai, C. L. Wu, M. T. Wu and D. B. Shieh, *Biomaterials*, 2005, **26**, 729–738.
41 H. T. Ta, Z. Li, C. E. Hagemeyer, G. Cowin, S. Zhang, J. Palasubramaniam, K. Alt, X. Wang, K. Peter and A. K. Whittaker, *Biomaterials*, 2017, **134**, 31–42.
42 H. Ta, Z. Li, C. Hagemeyer, G. Cowin, J. Palasubramaniam, K. Peter and A. Whittaker, *Atherosclerosis*, 2017, **263**, E146.
43 H. T. Ta, Z. Li, Y. Wu, G. Cowin, S. H. Zhang, A. Yago, A. K. Whittaker and Z. P. Xu, *Mater. Res. Express*, 2017, **4**, 11.
44 H. Ta, S. Prabhu, E. Leitner, F. Jia, K. Putnam, N. Bassler, K. Peter and C. Hagemeyer, *Atherosclerosis*, 2015, **241**, E26.
45 H. T. Ta, S. Prabhu, E. Leitner, F. Jia, D. von Elverfeldt, K. E. Jackson, T. Heidt, A. K. N. Nair, H. Pearce, C. von zur Muhlen, X. Wang, K. Peter and C. E. Hagemeyer, *Circ. Res.*, 2011, **109**, 365–373.
46 H. T. Ta, S. Prabhu, E. Leitner, F. Jia, K. Putnam, N. Bassler, K. Peter and C. Hagemeyer, *Circ. Res.*, 2010, **107**, e37–e38.
47 A. Tsourkas, V. R. Shinde-Patil, K. A. Kelly, P. Patel, A. Wolley, J. R. Allport and R. Weissleder, *Bioconjugate Chem.*, 2005, **16**, 576–581.
48 A. Mirshafiey and M. Mohsenzadegan, *Iran. J. Allergy, Asthma Immunol.*, 2008, **7**, 195–202.
49 S. M. Hirst, A. S. Karakoti, R. D. Tyler, N. Sriranganathan, S. Seal and C. M. Reilly, *Small*, 2009, **5**, 2848–2856.
50 D. Schubert, R. Dargusch, J. Raitano and S. W. Chan, *Biochem. Biophys. Res. Commun.*, 2006, **342**, 86–91.
51 A. Clark, A. P. Zhu, K. Sun and H. R. Petty, *J. Nanopart. Res.*, 2011, **13**, 5547–5555.
52 T. Shirai, M. Hilhorst, D. G. Harrison, J. J. Goronzy and C. M. Weyand, *Autoimmunity*, 2015, **48**, 139–151.
53 P. R. Taylor, L. Martinez-Pomares, M. Stacey, H. H. Lin, G. D. Brown and S. Gordon, *Annu. Rev. Immunol.*, 2005, **23**, 901–944.
54 R. W. Kinne, R. Brauer, B. Stuhlmuller, E. Palombo-Kinne and G. R. Burmester, *Arthritis Res.*, 2000, **2**, 189–202.
55 World Healyh Organization, Cardiovascular diseases (CVDs), http://www.who.int/mediacentre/factsheets/fs317/en/.
56 R. P. Patel, D. Moellering, J. Murphy-Ullrich, H. Jo, J. S. Beckman and V. M. Darley-Usmar, *Free Radical Biol. Med.*, 2000, **28**, 1780–1794.
57 H. Sakurai, H. Kohsaka, M. F. Liu, H. Higashiyama, Y. Hirata, K. Kanno, I. Saito and N. Miyasaka, *J. Clin. Invest.*, 1995, **96**, 2357–2363.
58 A. Karakoti, S. Singh, J. M. Dowding, S. Seal and W. T. Self, *Chem. Soc. Rev.*, 2010, **39**, 4422–4432.
59 J. M. Dowding, S. Das, A. Kumar, T. Dosani, R. McCormack, A. Gupta, T. X. T. Sayle, D. C. Sayle, L. von Kalm, S. Seal and W. T. Self, *ACS Nano*, 2013, **7**, 4855–4868.
60 C. Wilhelm, C. Billotey, J. Roger, J. N. Pons, J. C. Bacri and F. Gazeau, *Biomaterials*, 2003, **24**, 1001–1011.
61 L. K. Limbach, Y. C. Li, R. N. Grass, T. J. Brunner, M. A. Hintermann, M. Muller, D. Gunther and W. J. Stark, *Environ. Sci. Technol.*, 2005, **39**, 9370–9376.
62 S. Patil, A. Sandberg, E. Heckert, W. Self and S. Seal, *Biomaterials*, 2007, **28**, 4600–4607.
63 Y. Tabata and Y. Ikada, *Biomaterials*, 1988, **9**, 356–362.
64 C. J. Chen, H. Y. Lai, C. C. Lin, J. S. Wang and R. K. Chiang, *Nanoscale Res. Lett.*, 2009, **4**, 1343–1350.
65 V. V. Khutoryanskiy, A. V. Dubolazov, Z. S. Nurkeeva and G. A. Mun, *Langmuir*, 2004, **20**, 3785–3790.
66 J. T. Dahle, K. Livi and Y. Arai, *Chemosphere*, 2015, **119**, 1365–1371.
67 S. Bae, M. Park, C. Kang, S. Dilmen, T. H. Kang, D. G. Kang, Q. Ke, S. U. Lee, D. Lee and P. M. Kang, *J. Am. Heart Assoc.*, 2016, **5**, 11.
68 X. Liu, W. Wei, Q. Yuan, X. Zhang, N. Li, Y. Du, G. Ma, C. Yan and D. Ma, *Chem. Commun.*, 2012, **48**, 3155–3157.

Supporting Information for

Novel iron oxide-cerium oxide core-shell nanoparticle as a potential theranostic material for ROS related inflammatory diseases

Yuao Wu[a], Yanchen Yang[a], Wei Zhao[a], Zhi Ping Xu[a], Peter Little[d], Andrew K. Whittaker[a,b,c], Run Zhang[a], Hang T. Ta[a,b,d*]

[a]Australian Institute for Bioengineering and Nanotechnology, The University of Queensland, Brisbane, Australia

[b]Australian Research Council Centre of Excellence in Convergent Bio-Nano Science and Technology, Brisbane, Australia

[c]Centre for Advanced Imaging, the University of Queensland, Brisbane, Australia

[d]School of Pharmacy, the University of Queensland, Brisbane, Australia

*Correspondence to Hang T. Ta (h.ta@uq.edu.au)

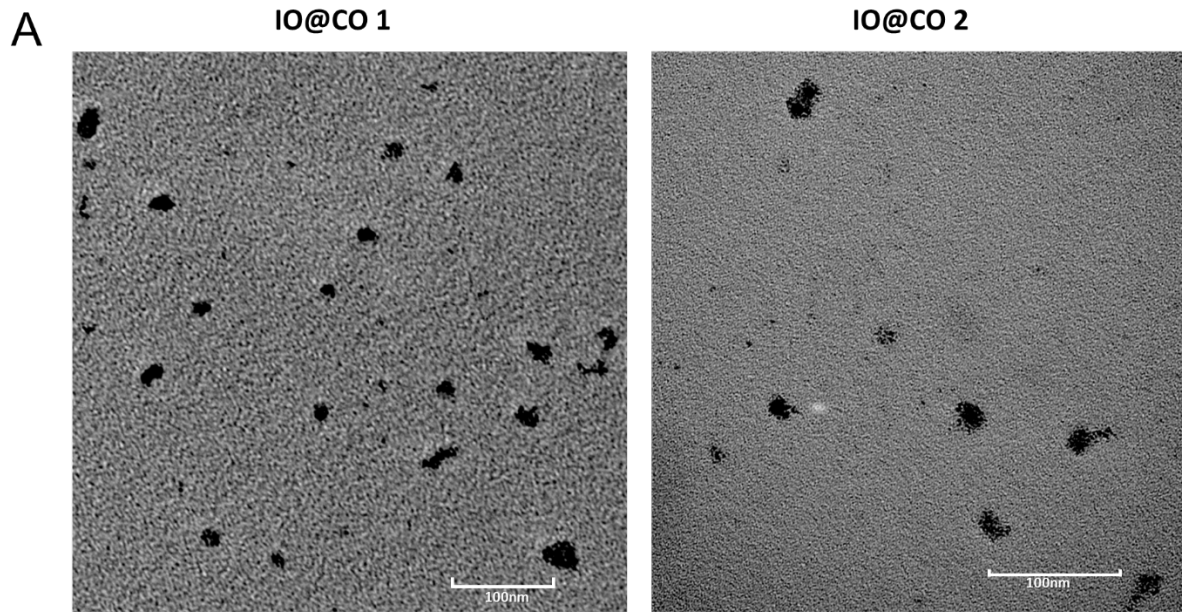

Figure S1. Low magnification TEM images IO@CO1 and IO@CO2 nanoparticles. Low magnification images showed the both distribution of IO@CO1 and IO@CO2 are good which corresponding to DLS data.

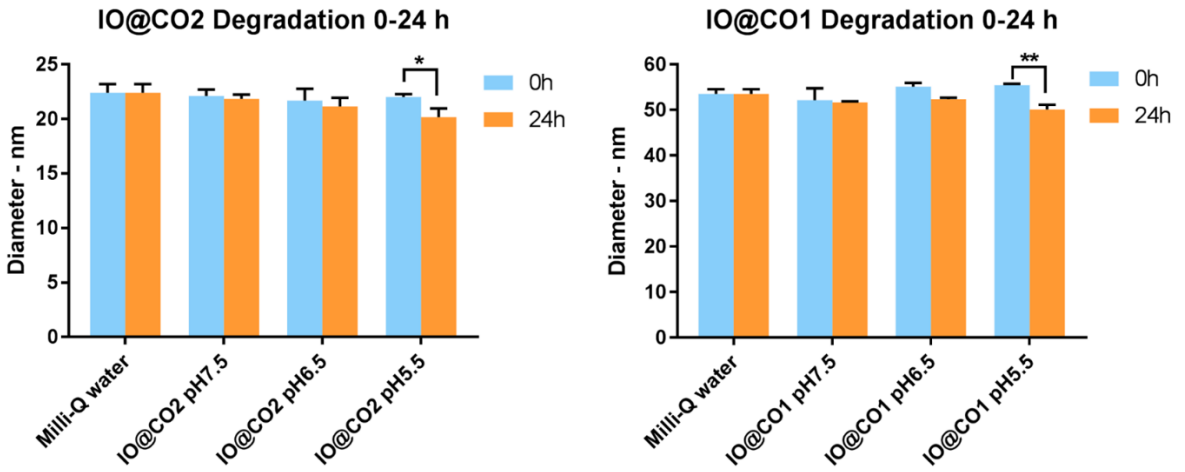

Figure S2. Degradation studies of IO@CO1 and IO@CO2. The Degradation studies showed both size of the IO@CO1 and IO@CO2 were decreased after 24hours treated by pH12 water.